

GJ 357: A low-mass planetary system uncovered by precision radial-velocities and dynamical simulations

J. S. Jenkins^{1,2*}, F. J. Pozuelos^{3,4,5}, M. Tuomi^{1,6}, Z. M. Berdiñas¹, M. R. Díaz¹,
J. I. Vines¹, Juan C. Suárez^{5,7}, P. A. Peña Rojas¹

¹*Departamento de Astronomía, Universidad de Chile, Camino El Observatorio 1515, Las Condes, Santiago, Chile, Casilla 36-D*

²*Centro de Astrofísica y Tecnologías Afines (CATA), Casilla 36-D, Santiago, Chile*

³*Space sciences, Technologies and Astrophysics Research (STAR) Institute, Université de Liège, 19C Allée du 6 Aout, B-4000 Liège, Belgium*

⁴*EXOTIC Lab, UR Astrobiology, AGO Department, University of Liège, 4000 Liège, Belgium*

⁵*Dpt. Física Teórica y del Cosmos, Universidad de Granada, Campus de Fuentenueva s/n, 18071, Granada, Spain*

⁶*Center for Astrophysics, University of Hertfordshire, College Lane Campus, Hatfield, Hertfordshire, UK, AL10 9AB*

⁷*Instituto de Astrofísica de Andalucía (CSIC), Glorieta de la Astronomía s/n, 18008, Granada, Spain*

Accepted 15th of October, 2019

ABSTRACT

We report the detection of a new planetary system orbiting the nearby M2.5V star GJ 357, using precision radial-velocities from three separate echelle spectrographs, HARPS, HiRES, and UVES. Three small planets have been confirmed in the system, with periods of 9.125 ± 0.001 , 3.9306 ± 0.0003 , and 55.70 ± 0.05 days, and minimum masses of 3.33 ± 0.48 , 2.09 ± 0.32 , and $6.72 \pm 0.94 M_{\oplus}$, respectively. The second planet in our system, GJ 357c, was recently shown to transit by the Transiting Exoplanet Survey Satellite (TESS; Luque et al. 2019), but we could find no transit signatures for the other two planets. Dynamical analysis reveals the system is likely to be close to coplanar, is stable on Myrs timescales, and places strong upper limits on the masses of the two non-transiting planets b and d of 4.25 and $11.20 M_{\oplus}$, respectively. Therefore, we confirm the system contains at least two super-Earths, and either a third super-Earth or mini-Neptune planet. GJ 357b & c are found to be close to a 7:3 mean motion resonance, however no libration of the orbital parameters was found in our simulations. Analysis of the photometric lightcurve of the star from the TESS, when combined with our radial-velocities, reveal GJ 357c has an absolute mass, radius, and density of $2.248^{+0.117}_{-0.120} M_{\oplus}$, $1.167^{+0.037}_{-0.036} R_{\oplus}$, and $7.757^{+0.889}_{-0.789} \text{gcm}^{-3}$, respectively. Comparison to super-Earth structure models reveals the planet is likely an iron dominated world. The GJ 357 system adds to the small sample of low-mass planetary systems with well constrained masses, and further observational and dynamical follow-up is warranted to better understand the overall population of small multi-planet systems in the solar neighbourhood.

Key words: stars: planetary systems; stars: activity; stars: low-mass; planets and satellites: detection; planets and satellites: dynamical evolution and stability

1 INTRODUCTION

In recent years, M dwarf planetary systems have shown themselves to exhibit a wide range in diversity, whilst also providing a rich hunting ground for instruments and teams with the capability to scrutinise them. The high impact discoveries of Proxima Centauri b (Anglada-Escudé et al. 2016) and Barnard’s Star b (Ribas et al. 2018) highlight this. The first planets found orbiting these stars through

radial-velocity (RV) measurements, started to hint at significant differences when compared to the populations of exoplanets that were emerging from the studies of Sun-like stars. For example, it was quickly observed that there appeared a relative lack of short-period gas giant planets (Bonfils et al. 2005; Johnson et al. 2010). This finding was explained as evidence for the core accretion model of planet formation, whereby large planets are more difficult to form orbiting small stars as they were likely orbited initially by much smaller proto-planetary disks (Laughlin et al. 2004). Yet, some features were also in agreement with stud-

* E-mail: jjenkins@das.uchile.cl

ies of planets orbiting more massive stars. Gas giant planets have been found in higher abundance orbiting Sun-like stars (Fischer & Valenti 2005; Adibekyan et al. 2012; Jenkins et al. 2017), and this bias appears to hold down into the M dwarf regime also (Schlaufman & Laughlin 2010; Rojas-Ayala et al. 2010; Montes et al. 2018).

One key feature that spurred the early efforts to search for planets orbiting M stars, was the fact that the biases work in favour of smaller planet detections. These stars could represent a pathway to studying the population of planets with masses below that of Neptune. Indeed, small planets began to appear in abundance orbiting M dwarfs (e.g. Bonfils et al. 2005; Forveille et al. 2009), and furthermore, it was witnessed that multi-planet systems were the norm, with a range of dynamically packed configurations beginning to appear (e.g. GJ 581, GJ 667C: Mayor et al. 2009; Anglada-Escudé et al. 2013). Large RV surveys of M stars have revealed that the planet fraction is around 100% (Bonfils et al. 2013; Tuomi et al. 2014). Furthermore, the occurrence rate of planets in these systems is also high, particularly in the stellar habitable zone, with a rate of $0.21^{+0.03}_{-0.05}$ planets per star with masses between 3–10 M_{\oplus} (Tuomi et al. 2014).

More recently, transit surveys have also turned towards M stars as prime targets in their quest for ever smaller exoplanets. The transit bias works in a similar manner to the RV bias, such that small stars allow the detection of smaller planets as the transit dip has a high signal-to-noise ratio. TRAPPIST-1 (Gillon et al. 2017) was a prime example of the type of planet systems that small M stars can host. Transits from seven small rocky planets on short period orbits were found, allowing detailed studies to be conducted on the possible atmospheres and their constituents of small planets orbiting a single star, and hence with similar initial conditions (e.g. Alberti et al. 2017; Ducrot et al. 2018; Moran et al. 2018; Miles-Páez et al. 2019; Burdanov et al. 2019).

Recent, instrumentation in space has allowed an even deeper study of the population of planets orbiting small stars. The Kepler Space Telescope (Borucki et al. 2010) observed thousands of M stars in its viewing zone, and revealed similar statistical constraints to that of the RV studies. Kopparapu (2013) used their own updated prescriptions for the extent of the conservative and optimistic habitable zones, to reveal occurrence rates of $0.48^{+0.12}_{-0.24}$ and $0.53^{+0.08}_{-0.17}$ planets per star, respectively. Dressing & Charbonneau (2015) found 159 planet candidates, revealing an occurrence rate of 2.5 ± 0.2 planets per star with radii 1–4 R_{\oplus} and orbital periods less than 200 days. They also found a higher rate for the smallest planets, but in radius not mass. Within orbital periods of 50 days, planets with radii 1–1.5 R_{\oplus} have an occurrence rate of $0.56^{+0.06}_{-0.05}$ planets per star, whereas those with radii 1.5–2.0 R_{\oplus} have a rate of $0.46^{+0.07}_{-0.05}$ planets per M star.

The latest space mission that will study a wider sample of M stars is the Transiting Exoplanet Survey Satellite (TESS) project (Ricker et al. 2015). According to simulations, TESS will find 990 ± 350 planets among 715 ± 255 early-to-mid M dwarf host stars (Ballard 2019). One key goal of TESS, a Level 1 science goal, is to provide constrained radii and masses for 50 planets below 4 R_{\oplus} . In this work, we discuss a rich planetary system orbiting the M star

Table 1. Some key stellar parameters for GJ 357.

Parameter	Value	Source
TESS Names	TIC413248763 (TOI-562)	
RA [hr:min:secs]	09:36:01.63725	Gaia
Dec [deg:min:sec]	-21:39:38.87828	Gaia
Parallax [mas]	105.8830 ± 0.0569	Gaia
Distance [pc]	19.5485 ± 0.0106	Gaia
V [mag]	10.91 ± 0.02	Hipparcos
SpT	M2.5V	N14
T_{eff} [K]	3344 ± 110	N14
$\log g$ [cm s^{-2}]	4.906 ± 0.062	St18
[Fe/H] [dex]	-0.30 ± 0.09	N14
L/L_{\odot}	0.0175 ± 0.0011	St18
R/R_{\odot}	0.359 ± 0.011	Mu18
M/M_{\odot}	0.378 ± 0.03	Mu18
$v \sin(i)$ [kms^{-1}]	1.21	H17
$P/\sin(i)$ [days]	18.7 ± 4.3	H17
$\log R'_{HK}$ [dex]	-5.652	H17

Gaia: Gaia Collaboration et al. (2016, 2018); Hipparcos: Perryman et al. (1997); H17: Houdebine et al. (2017); Mu18: Muirhead et al. (2018); N14: Neves et al. (2014); St18: Stassun et al. (2018) .

GJ 357, with one such candidate found to transit its star (see Luque et al. 2019). The mass and radius of this transit candidate makes the system a TESS Level 1 science target. GJ 357 is located within 20 pc of the Sun, and is an early-M star that is on the main sequence. The star has a mass and radius of $0.378 \pm 0.03 M_{\odot}$ and $0.359 \pm 0.011 R_{\odot}$, respectively, and is found to be inactive and metal-poor ([Fe/H] = -0.30 ± 0.09 dex). The main stellar parameters that we are interested in for this work are listed in Table 1.

The paper is formatted as follows: in § 2 we discuss the RV detection of our planetary system, along with the properties of the host star. In § 3 we discuss the stellar activity analysis we performed to rule out activity as the source of the signals, whilst in § 4 we show the TESS light curve and discuss the joint model that provides our overall constraints on the planetary system. Finally, in § 6 we discuss the impact of this result and summarise our findings.

2 RV CANDIDATES

GJ 357 was a target star in the Zechmeister et al. (2009), Bonfils et al. (2013), Tuomi et al. (2014) and Tuomi et al. (2019) samples studying the RV variability of nearby M dwarfs. Tuomi et al. (2019) reported three candidate planets orbiting the star based on an analysis of combined HARPS, HiRES, and UVES radial velocities. We revisit the detections of the corresponding signals in this section and the data analysed in Tuomi et al. is referred to as the “old data”.

As discussed by Feng et al. (2017), RVs calculated for independent spectrograph orders can be used as independent data sets. We have used the HARPS RVs for each of the independent 72 orders to calculate the radial velocity data sets as in Anglada-Escudé & Butler (2012), but we have also obtained independent velocity sets by dividing the 72 HARPS orders into three subsets of 24 orders, and by neglecting the first such subset because it corresponds to the noisiest velocities calculated for the bluest wave-

lengths (Anglada-Escudé & Butler 2012). Consequently, we have two data sets obtained for HARPS orders 25-48 and 49-72 that can be used as independent RV data sets in the analyses. Moreover, we have analysed these sets in combination with data from other instruments, including a new reduction of UVES velocities, and accounted for the wavelength-dependent variability in these sets by using the so-called differential velocities as noise proxies (Feng et al. 2017). We refer to this data as the “new data”.

The combined RV data of GJ 357 (old and new) was analysed by applying the delayed-rejection adaptive Metropolis (DRAM) Markov chain Monte Carlo (MCMC) algorithm (Haario et al. 2001, 2006) that is a generalised version of the Metropolis-Hastings posterior sampling algorithm (Metropolis et al. 1953; Hastings 1970) and has been applied in e.g. Butler et al. (2017), Díaz et al. (2018), and Tuomi et al. (2018). This sampling technique was applied in two steps (see e.g. Tuomi et al. 2019). First, for a model with $k \geq 1$ Keplerian signals, we performed searches for periodic signals by obtaining a sample from the posterior probability density in order to identify what signal periods correspond to the highest probability maxima in this density. In the second step, we obtained statistically representative samples from the joint posterior density of model parameters by starting the corresponding samplings at or near the highest probability maximum in the period space. The obtained results were then subjected to statistical tests in order to determine whether the identified probability maxima corresponded to statistically significant signals (see e.g. Tuomi et al. 2019). We calculated the Bayesian information criterion for each model with different numbers of Keplerian signals to estimate the significances of signals because of its simplicity (Liddle 2007) and robustness in practice (Feng et al. 2016).

Three clear periodic signals were identified in the combined RV data as reasonably unique solutions in the period space between 0.5 days and combined data baseline of 5500 days (Fig. 1). These signals satisfy our signal detection criteria (Tuomi et al. 2014) in the sense that they correspond to significant improvements to the model and have parameters, namely amplitude K and period P , that are well-constrained from above and below (see e.g. Tuomi 2011; Tuomi et al. 2014). We illustrate the uniqueness of these signals in Fig. 1 and describe their significances in Table 2.

As can be seen in Table 2, although the signals correspond to unique maxima in the period space (Fig. 1), only one signal is detected robustly in the old data such that there is *strong evidence* for it according to the requirement of Kass & Raftery (1995) that the model is 150 times more probable than its rival. Yet, if we assume circular orbits, all three signals are detected for the old data significantly as well. We also demonstrate in Table 2 and Fig. 1 that three signals are detected credibly in the new data set. As can be seen, it is clear that when we treat the velocities calculated for independent subsets of orders as independent data sets, this greatly enhances the significance (Table 2) of the signals, for instance revealing the presence of the 55 d signal after modelling only the first Keplerian signal (see Fig. 1). We also note that all three signals are supported by i) all instruments and ii) RVs calculated for both wavelength ranges of the HARPS instrument. This implies that the signals are i) independent of instrument and ii) wavelength-invariant, demonstrating that they are unlikely

Table 2. Logarithms of maximum likelihood values $\log L(k)$ and estimated model probabilities $P(k)$ given all the data assuming equal *a priori* probabilities for models with k Keplerian signals. The table contains model comparisons for the old data sets of (Tuomi et al. 2019) as well as for analyses where the new UVES data reduction is used together with division of HARPS data into independent time-series for different wavelength intervals (new data). The last column denotes the (potential) period P_k of the k th signal.

k	Old data		New data		P_k (days)
	$\log L(k)$	$P(k)$	$\log L(k)$	$P(k)$	
0	-425.43	3.1×10^{-6}	-531.39	1.2×10^{-19}	–
1	-403.13	0.051	-500.90	3.7×10^{-12}	9.1
2	-388.78	0.293	-478.98	2.1×10^{-8}	3.9
3	-375.45	0.612	-451.58	0.029	55.7
4	-365.48	0.045	-434.79	0.971	34.0

to have been caused by biases in instrumentation or colour-dependent stellar variability associated with stellar activity (see Tuomi et al. 2018). We also note that the potential existence of a fourth signal at a period of 34 days (see Table 2) should be investigated when more data becomes available.

We have presented evidence for three unique and significant signals in the combined radial velocity data of GJ 357 at periods of 9.12462 ± 0.00127 , 3.93055 ± 0.00025 and 55.698 ± 0.045 days, where the uncertainties correspond to the standard errors. The Keplerian parameters and the inferred minimum masses and semi-major axes are tabulated in Table 3 based on the new data set.

In order to help validate our results, we performed an independent test of the reality of the system by running the Exoplanet Mcmc Parallel tEmpering Radial velOCity fitteR **EMPEROR**¹ (Peña Rojas & Jenkins 2019) automatic signal detection code. **EMPEROR** employs a similar statistical model to the DRAM approach, except the exponential moving average smoothing time-scale is left as a free parameter, and in this case we also used a first-order moving average correlated noise model. The main difference between the two methods is that **EMPEROR** performs the MCMC samplings by using parallel tempering methods across multiple simultaneous chains (five in this case), each one hotter (with smaller $\beta < 1$ such that likelihood function l^β is used rather than l) than the next. It uses the **EMCEE** code (Foreman-Mackey et al. 2013) as the basis for the samplings in this respect. The statistical model is taken from the cold chain ($\beta = 1$). We employed 150 walkers and 15'000 steps per chain, meaning we obtain a chain length of 11.25M, along with half that value used as burn-in, allowing **EMPEROR** to thoroughly explore the high dimensional posterior parameter space. **EMPEROR** yields a similar solution to the DRAM samplings for the outer two planet candidates, arriving at the 55 day planet signal first, followed by the 9 day planet signal next. The transiting 3 day planet signal was not detected in the automatic runs, (by automatic runs we mean the basic **EMPEROR** operational format where the code runs alone by modifying the priors for each model test, testing the Bayesian significances, for example,

¹ <https://github.com/ReddTea/astroEMPEROR>

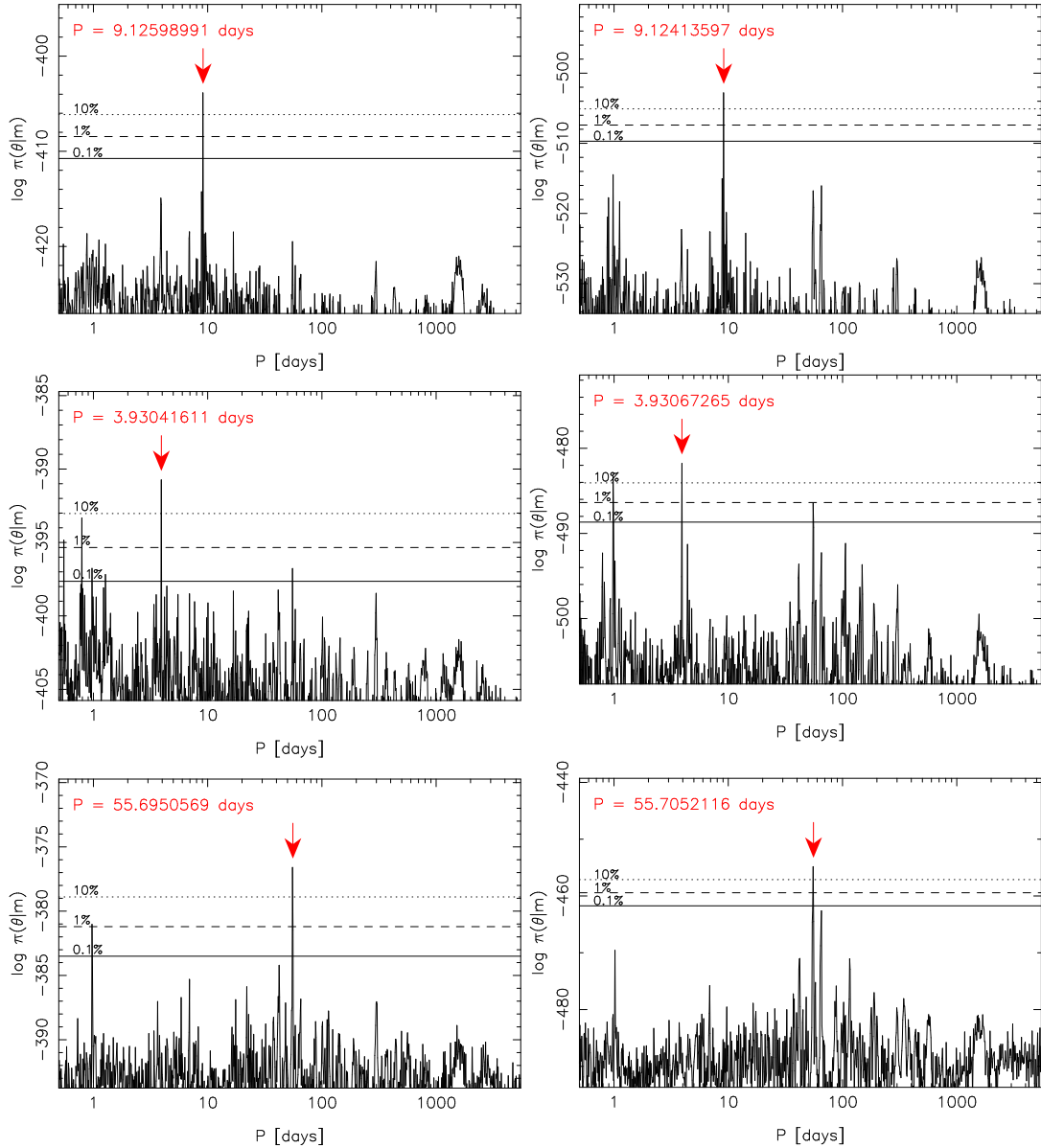


Figure 1. Estimated posterior probability density based on DRAM samplings of models with $k = 1, 2, 3$ Keplerian signals as a function of the period parameter of the k th signal (top to bottom). The red arrow indicates the position of the global maxima in the period space and the horizontal lines denote the 10% (dotted), 1% (dashed), and 0.1% (solid) equiprobability thresholds with respect to the maxima. The left (right) hand side panels denote the posteriors given the old (new) data (see text).

without any human intervention), meaning we confirm the existence of the two outer signals, but could not confirm the RV signal from the transiting planet.

3 STELLAR ACTIVITY ANALYSIS

3.1 Spectroscopic Activity indices

In order to test the true planetary nature of the signals found in the RVs, we analysed the spectral activity indices derived from the available spectra. First, for the HARPS data we computed the activity indices using the HARPS-TERRA algorithm (Anglada-Escudé & Butler 2012). The full-width at half maximum (FWHM) of the cross-correlation function (CCF) and the bisector inverse slope (BIS) are read directly

from the fits headers obtained as a product of the HARPS online data reduction software (DRS). The rest of the activity indices, i.e. S-index, H_{α} , Na I, Na II, are not provided as a standard product of the DRS and thus are computed from the one dimensional reduced spectra. For instance, the S-index values that are calculated by studying the cores of the Calcium II H & K lines (e.g. Jenkins et al. 2008, 2011; Sousa et al. 2011), are calibrated to the Mount Wilson system for direct comparison to other stars, giving rise to a proxy for the chromospheric activity variability of the star.

We ran a Generalized Lomb-Scargle (GLS; Zechmeister & Kürster 2009) periodogram on each of the activity indices time series. For each periodogram we defined a pseudo-Nyquist frequency $\omega_{\max} = \pi/\Delta T$, i.e., the largest frequency this analysis is sensitive to. ΔT

Table 3. Maximum *a posteriori* estimates, standard errors and 99% Bayesian credibility intervals of the Keplerian parameters and candidate masses given a model with three Keplerian signals and the new data set. The parameters are the Keplerian amplitude K , period P , eccentricity e , the longitude of pericentre ω , mean anomaly M_0 , minimum mass $m \sin i$, and semi-major axis a . The uncertainties of minimum masses and semi-major axes have been estimated by accounting for the uncertainty in the stellar mass.

	GJ 357 b	GJ 357 c	GJ 357 d
K (ms^{-1})	2.20 ± 0.25 [1.54, 2.95]	1.84 ± 0.23 [1.18, 2.51]	2.41 ± 0.32 [1.52, 3.31]
P (days)	9.1246 ± 0.0013 [9.1207, 9.1279]	3.93055 ± 0.00025 [3.92981, 3.93129]	55.698 ± 0.045 [55.555, 55.826]
e	0.072 ± 0.053 [0, 0.240]	0.047 ± 0.059 [0, 0.267]	0.033 ± 0.057 [0, 0.259]
ω (rad)	5.3 ± 1.9 [0, 2π]	3.9 ± 1.3 [0, 2π]	0.3 ± 2.2 [0, 2π]
M_0 (rad)	4.3 ± 1.8 [0, 2π]	5.8 ± 2.2 [0, 2π]	5.3 ± 2.0 [0, 2π]
$m \sin i$ (M_{\oplus})	3.68 ± 0.48 [2.35, 5.14]	2.32 ± 0.33 [1.40, 3.24]	7.20 ± 1.07 [4.39, 10.33]
a (AU)	0.0607 ± 0.0021 [0.0544, 0.0664]	0.0348 ± 0.0012 [0.0310, 0.0379]	0.2040 ± 0.0069 [0.1820, 0.2218]

is the median spacing between data points in the time series. We also defined our optimal minimum frequency by $\omega_{\min} = 2\pi/T_{\max}$, with T_{\max} the time span of the time series. We defined our grid of frequencies by setting the spacing as $\Delta\omega = \eta\omega_{\min}$, with $\eta = 0.1$. Finally the number of sample frequencies to test is $n_{\omega} = (\omega_{\max} - \omega_{\min})/\Delta\omega$.

Figure 2 shows the results of the GLS periodogram for the activity indices described before. No statistically significant power peaks are found in the power spectrum of BIS, FWHM, and Na II. We note that the reason for the lack of a signal in the BIS and FWHM indices may be due to the general lack of any well constrained continuum region for HARPS M dwarf CCFs, a noise source that could mask any signal present (e.g. see Fig. 7 in Berdiñas et al. 2017). From the periodogram of H_{α} significant powers are found at ~ 75 and ~ 115 days. The S-index periodogram shows a significant power above the 0.1% significance level at ~ 73 days. Na I, on the other hand, exhibits power peaks above the 1% significance level at ~ 120 and ~ 150 days. Similar values were reported by Astudillo-Defru et al. (2017) ($P_{\text{rot}} = 144$ d) and Schöfer et al. (2019) ($P_{\text{rot}} = 74.3$ d). We believe that the S-indices here are probing the primary rotation period of the star, with a periodicity in good agreement with that presented in (Luque et al. 2019) using both photometric and spectroscopic activity measurements. Beyond these standard indices we also perform the same analysis on our new colour dependent differential velocity indices (Fig. 3), revealing no significant periods.

3.2 ASAS Photometry

We searched for photometric measurements of the star from the All-Sky Automated Survey (Pojmanski 1997) catalog. We found 644 measurements consisting of V -band photometry spanning ~ 9 years, from Nov 20th 2000 to Nov 29th 2009. We filter the photometry by selecting the highest quality data, flagged as ‘‘A’’ and ‘‘B’’. After filtering out 54 bad data points, we analyse 587 photometric measurements to search for stellar rotational periods. Figure 4 shows the GLS periodogram of the photometry showing no statistical significant power peaks to constrain P_{rot} for this star.

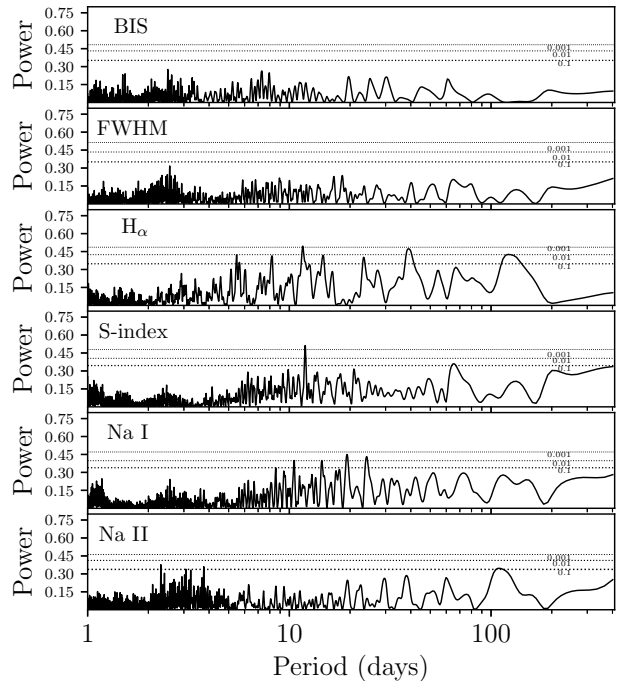


Figure 2. Top to bottom: Generalized Lomb-Scargle periodogram for the BIS, CCF-FWHM, H_{α} , S-index, Na I and Na II derived from the spectra using the HARPS-TERRA reduction package. Dotted lines, from bottom to top, represent the 10, 1 and 0.1% significance levels computed by running 5000 bootstrap iterations.

4 TESS CONFIRMATION

The TESS is a NASA-sponsored Astrophysics Explorer-class mission that is performing a wide-field survey to search for planets transiting bright stars (Ricker et al. 2015). It has four $24 \times 24^\circ$ field of view cameras with four $2\text{k} \times 2\text{k}$ CCDs each, with a pixel scale of 21 arcseconds per pixel and a bandpass of 600-1000 nm. GJ 357 was observed by TESS in Sector 8 using CCD 3 of Camera 2 between February 2nd and 27th 2019.

The TESS data of GJ 357 were obtained from the

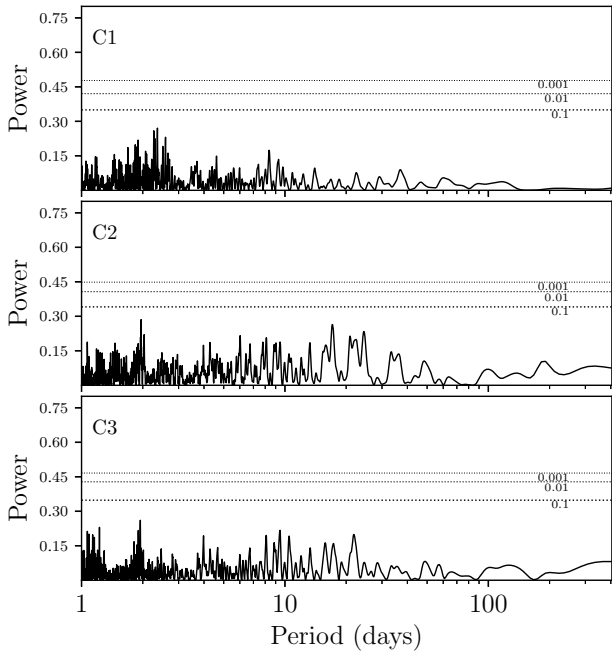


Figure 3. *Top to bottom:* Generalized Lomb-Scargle periodogram of the colour dependent differential velocities derived from the HARPS spectra using the HARPS-TERRA software. Dotted lines, from bottom to top, represent the 10, 1 and 0.1% significance levels computed by running 5000 bootstrap iterations.

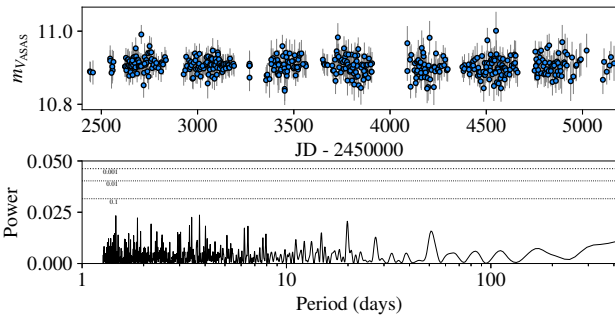


Figure 4. *Top:* V-band ASAS photometry for GJ 357. *Bottom:* Generalized Lomb-Scargle periodogram of the photometry. Dotted lines correspond, from bottom to top, to the 10, 1 and 0.1% significance levels computed via 5000 bootstrap iterations on the original photometry time series.

NASA Mikulski Archive for Space Telescopes (MAST)². We downloaded the corresponding Target Pixel (TP) file provided for our target. This TP file contains raw and calibrated fluxes in an image cube of 15×15 pixels observed with a two-minute temporal cadence. After removing cadences affected by instrumental issues and marked with non-zero “quality” flags, the temporal dimension of the cube comprised 13392 epochs. The top panel of Fig. 5 shows the light curve obtained by performing simple aperture photometry. The aperture was defined by the pixels with flux above the

85 th percentile of the median image calculated along the time axis.

The observations of GJ 357 were paused during the spacecraft perigee passage to download the data. Observations should have been resumed soon after, but an interruption in communications between the instrument and spacecraft caused a final ~ 6 days gap in the light curve (JD=241529.06–241535.00). Also, the need of turning on the camera heaters after the communications failure caused a small drift in the star position due to changes in the camera focal plane (see the star drift at the bottom panels of Fig. 5). As a consequence, the light curve shows a progressive increase of the flux after resuming the observations. The flux returned to nominal within a few days.

We tried different apertures to mimic this effect as well as a simple spline fitting, but finally we decided to use the Presearch Data Conditioning (PDC) flux given by the Science Processing Operations Center (SPOC, Jenkins et al. 2016) at MAST public archive. The PDC pipeline was first implemented for *Kepler* to account for systematics error sources from either the telescope or the spacecraft, such as focus changes, sudden pixel sensitivity dropouts, pointing drifts, and thermal transients. The second panel of Fig. 5 shows the normalised PDC light curve resulting after discarding high-dispersion epochs with a 4-sigma criteria. Besides the transit features of the inner planet (marked with red arrows), the PDC light curve shows evident long term variabilities. We smoothed the light curve with a Savitzky-Golay filter (Savitzky & Golay 1964). The third panel of Fig. 5 shows the final detrended light curve. Although there are three stars within TESS pixel size of $21''$, our target star and two other Gaia sources, these background contaminants are around 7 magnitudes fainter in the optical, rendering their contamination factor small. In Luque et al. (2019) they also considered the effect these background stars would have on the TESS lightcurves, in order to determine the dilution factor needed to correct for this effect and calculate the proper planetary radius. They found a value consistent with zero, therefore no dilution correction is necessary.

This light curve was used to perform a joint photometry and RV model fit using *Juliet* (Espinoza et al. 2018). *Juliet* is a Python tool designed to analyse transits, RVs or both simultaneously, allowing for multiple photometry and RV instruments to be modelled at the same time. It calculates the Bayesian Evidence of the model with the use of Nested Sampling, Importance Nested Sampling, or Dynamic Nested Sampling algorithms (Feroz et al. 2009; Buchner et al. 2014), sampling the posterior parameter space as a by-product. For the light curve model, *Juliet* employs *batman* (Kreidberg 2015). The Keplerian model is provided by *RadVel* (Fulton et al. 2018). *Juliet* also allows the use of Gaussian Processes to model the photometry and RVs. In this work we used a Matern multiplied by exponential kernel from *celerite* to fit the photometry (Foreman-Mackey et al. 2017). We considered two different models for the joint photometry and RV fit: one with free eccentricity and another with the eccentricity fixed to 0; adopting the same thresholds for weak and strong evidence as in Espinoza et al. (2018) ($\Delta \ln Z = 2$ and $\Delta \ln Z = 5$ respectively). We found that $\Delta \ln Z = 9.676$ in favour of the fixed eccentricity model and thus we selected it as our final solution. We show the TESS light curve transit event in

² http://archive.stsci.edu/tess/bulk_downloads/bulk_downloads_final_solution.html

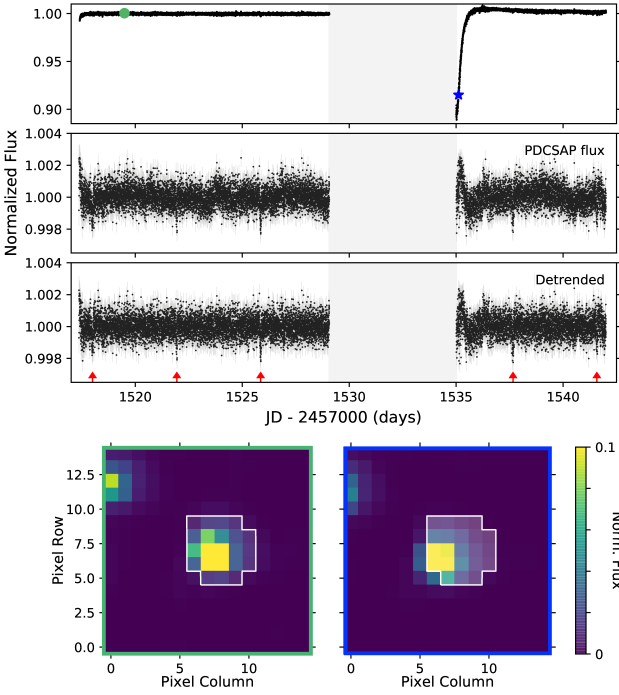


Figure 5. *Top:* GJ 357 TESS light curve obtained with aperture photometry from calibrated pixels given in the Target Pixel files. The grey area highlights ~ 6 days of no observations (see text for details). *Second:* Normalised PDC photometry without 4-sigma outliers. *Third:* Final PDC light curve after accounting for the long-term variability. The red arrows indicate the transit times of GJ 357 c. *Bottom:* Target Pixel files at epochs 2458519.49 (left; green frame) and 2458535.11 days (right; blue frame) corresponding to the green dot and a blue star in the top panel. The shaded white areas indicate the aperture used to get the light curve in the top panel.

Table 4. Planetary Properties for GJ 357 c

Property	Value
P (days)	3.93086 ± 0.00004 [3.93050, 3.93101]
T_C (BJD - 2450000)	8517.9994 ± 0.0001 [8517.9985, 8518.0004]
a/R_*	$20.165^{+0.155}_{-0.190}$ [17.707, 20.643]
b	$0.529^{+0.010}_{-0.005}$ [0.514, 0.600]
K (ms^{-1})	$1.7372^{+0.0054}_{-0.0007}$ [1.7356, 1.7539]
e	0 (<i>fixed</i>)
M_p (M_\oplus)	$2.248^{+0.117}_{-0.120}$ [1.930, 2.547]
R_p (R_\oplus)	$1.167^{+0.037}_{-0.036}$ [1.073, 1.264]
ρ_p (gcm^{-3})	$7.757^{+0.889}_{-0.789}$ [5.867, 10.295]
a (AU)	0.033 ± 0.001 [0.028, 0.036]
i (deg)	$88.496^{+0.025}_{-0.043}$ [88.063, 88.561]

Values inside the square brackets represent the 99% posterior estimates from the joint modeling.

Figure 6 and the resulting parameters for GJ 357 c in Table 4.

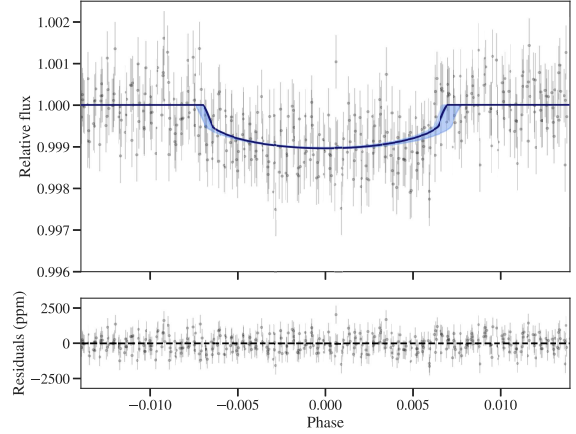


Figure 6. Phase folded TESS photometry. The solid blue line is the best fit for the photometry and the blue shaded regions represent the 1, 2, 3 σ confidence levels. Bottom: The residuals of the fit in ppm.

5 ORBITAL DYNAMICS

With the RV data and photometric TESS observations it is possible to perform a first full characterisation that includes planetary dynamics and orbital analysis. In particular, we sought to constraint the mass of the components and their mutual inclinations. In addition, we studied the global stability of the system in order to provide the most likely dynamical configuration.

5.1 The impact parameters of planets GJ 357b and GJ 357d

Since only the innermost planet GJ 357c is transiting, we wonder about the inclinations of the outermost planets GJ 357b and GJ 357d. In transiting exoplanets, the impact parameter, b , is the sky-projected distance conjunction, in units of stellar radius (e.g., Winn 2010):

$$b = \frac{a \cos i}{R_*} \left(\frac{1 - e^2}{1 + e \sin \omega} \right), \quad (1)$$

where a is the semimajor axis, i is the orbital inclination, R_* is the radius of the star, e is the eccentricity and ω is the longitude of pericenter. The b -parameter varies from $b = 0$, when the planet cross the centre of the stellar disk, and $b = 1$, when it is on the cusp of the disk. We analysed the b -parameter for the two outermost planets to search for the maximum inclinations that make these planets non-transiting. For each planet, we analysed both circular and eccentric orbits, where the chosen eccentric orbits were the nominal values provided in Table 3, i.e., $e_b=0.072$ and $e_d=0.033$. We find that planet GJ 357 b has a maximum inclination ranging between $88.5^\circ - 88.4^\circ$. For planet GJ 357 d, we found that the maximum angle is $\sim 89.5^\circ$. Since the inclination found by the analysis of the TESS lightcurve for the inner planet GJ 357 c is $i \sim 88.49^\circ$, we note that even a near-coplanar configuration makes the two outer planets non-transiting (see Fig. 7). This may explain the lack of

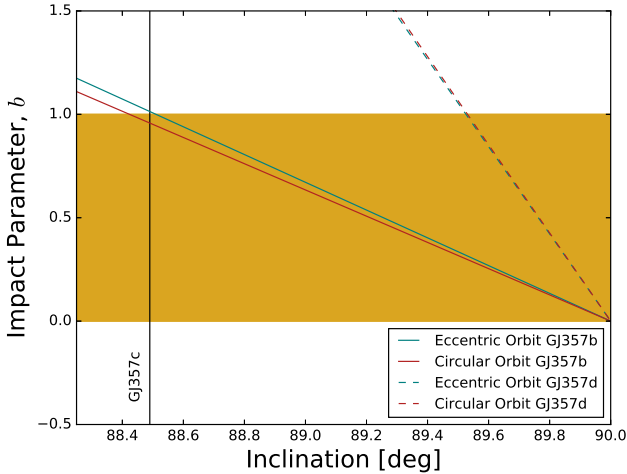


Figure 7. Impact parameters of planets GJ 357 b and GJ 357 d for different inclinations according to equation 1. Both eccentric (blue line) and circular (red line) orbits are shown, given from the values determined by the radial-velocity solution. The yellow-shaded region delimits the solutions allowed for each planet to transit its host star, and the vertical line marks the inclination of the transiting planet GJ 357 c.

transit signals for planets GJ 357 b and GJ 357 d in TESS data.

In fact, the general belief is that planets tend to reside in nearly coplanar orbits within a few degrees of inclination from an inertial plane perpendicular to the total angular momentum of the system. For example, in the Solar System, the highest inclination is obtained for Mercury, which has $i \sim 7^\circ$. This hypothesis is also supported observationally. Indeed, the combination of *Kepler* and HARPS data suggest that the mutual inclinations of multi-planet systems are $\lesssim 5^\circ$ (see e.g., Fabrycky et al. 2014; Tremaine & Dong 2012; Figueira et al. 2012). However, while stellar and planetary formation theories require an accretion disk perpendicular to the total angular momentum of the system in which planets form, close encounters and/or captures in mean motion resonances (MMRs) orbits might significantly increase their eccentricities and inclinations (e.g., Lee et al. 2007; Libert & Tsiganis 2009b). With this in mind, we conducted dynamical simulations to explore the minimum values of the inclinations for planets GJ 357 b and GJ 357 d. Furthermore, their masses are dependent on their orbital inclination angles, which means that any uncertainties in the inclination angles will seriously affect their determined masses. Hence, exploring the minimum values of their inclination angles is equivalent to exploring the maximum values of their masses.

5.2 The MEGNO criterion and short-term stability

We study the short-term stability of the system through the Mean Exponential Growth factor of Nearby Orbits, $Y(t)$ (MEGNO, Cincotta & Simó (1999, 2000); Cincotta et al. (2003)). MEGNO is a chaos index that has been extensively used within dynamical astronomy, in both the Solar System and extrasolar planetary systems (e.g., Jenkins et al. 2009;

Hinse et al. 2010; Contro et al. 2016; Günther et al. 2019). It allows us to explore the whole parameter space at small computational cost. In brief, MEGNO evaluates the stability of a body’s trajectory after a small perturbation of the initial conditions. Its time-averaged mean value, $\langle Y(t) \rangle$, amplifies any stochastic behaviour, allowing the detection of hyperbolic regions during the integration time. Therefore, $\langle Y(t) \rangle$ allows us to distinguish between chaotic and quasi-periodic trajectories: if $\langle Y(t) \rangle \rightarrow \infty$ for $t \rightarrow \infty$ the system is chaotic; while if $\langle Y(t) \rangle \rightarrow 2$ for $t \rightarrow \infty$ the motion is quasi-periodic. We used the MEGNO implementation within the N-body integrator REBOUND (Rein & Liu 2012), which made use of the Wisdom-Holman WHfast code (Rein & Tamayo 2015). We evaluated the inclination 1000 times between 88.5° and 0.1° for both planets by considering circular and eccentric orbits (see Fig. 8). The integration time was set to 10^6 times the orbital period of the outermost planet, GJ 357 d. The time-step was set to 5% of the orbital period of the innermost planet, GJ 357 c. In order to prevent unnecessary computations, we prematurely terminated any integration when one of the planets was ejected from the system, where we consider an ejection cases when the semimajor axis of a given planet reaches values larger than 20 AU, hinting at clear chaotic behaviour.

Using the method outline, we firstly evaluated the inclination of the planet GJ 357 b by assuming the (fixed) planetary parameters given in Tables 3 and 4, and considered co-planar orbits between GJ 357 c and GJ 357 d. We find that planet GJ 357 b becomes unstable when the inclination is less than or equal to $\sim 56^\circ$ for eccentric orbits with $e_b = 0.072$, and $\sim 53^\circ$ or less for circular orbits. Secondly, we explored the outermost planet GJ 357 d, and held constant the values of planet GJ 357 c and GJ 357 b (given in Tables 3 and 4), considering coplanar orbits. Since planet GJ 357 d is very far from the two innermost planets, it is expected to withstand lower inclinations. Indeed, we find that for eccentric orbits of $e_d = 0.033$, the minimum inclination is $\sim 32^\circ$, and for circular orbits, it is $\sim 26^\circ$.

From these sets of simulations, we note that in the nearly co-planar scenario, the stability of the system is mainly controlled by the two innermost planets GJ 357 c and GJ 357 b, while the outermost planet GJ 357 d is too distant to induce perturbations. However, while planet GJ 357 c is strongly characterised by the synergy of both the RV and photometric measurements, planet GJ 357 b is only characterised through its RV. Hence, we wonder if in the range of uncertainties obtained for planet GJ 357 b, the system could actually be fully stable. To address this question we constructed a two-dimensional MEGNO-map in the $e_b - a_b$ parameter space. The integration time and the time-step are the same as used before. In order to reduce the computation time, we checked the integration every 1000 yr, and we chose to stop a given integration when $\langle Y(t) \rangle > 5$ (Hinse et al. 2015). The size of the obtained MEGNO-map was 200×200 pixels, meaning we explored the $e_b - a_b$ parameter space for planet GJ 357 b up to 40,000 times (Fig. 9). We find that planet GJ 357 b seems to be fully stable in the 1σ uncertainty space (inner red-box), but some instabilities might be found when we extend to the 2σ uncertainty space (outer red-box), which mostly corresponds to larger values of e_b . This result suggests that in terms of stability,

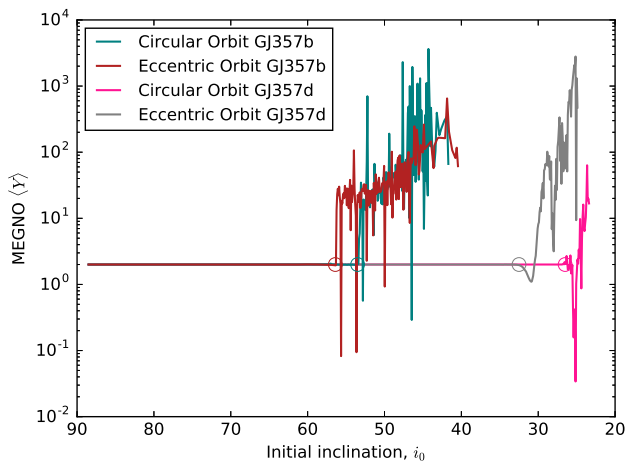


Figure 8. Stability analysis based on the MEGNO chaos index for different inclinations of planets GJ 357 b and GJ 357 d. Both eccentric and circular orbits are explored for 1000 initial inclination angles ranging from 88.5° to 0.1° . The systems are stable while $\langle Y(t) \rangle \rightarrow 2$, and become unstable as $\langle Y(t) \rangle$ diverge from 2. The circles over the horizontal lines give the angles stable while $\langle Y(t) \rangle \rightarrow 2$, i.e., when the system is no longer stable.

planet GJ 357 b favours low eccentricity values in terms of the radial velocity orbital solution.

However, an alternative configuration to the nearly coplanar scenario is still possible. Indeed, planets GJ 357 b and GJ 357 c are close to a MMR of 7:3, i.e. a high-order resonance of $q=4$. [Libert & Tsiganis \(2009a\)](#) suggested that high-order resonances might provoke an excitation of inclinations angles, where the maximum mutual inclinations range between 20° and 70° . This may explain why planet GJ 357 b is not transiting: the two inner planets are trapped in an inclination-type resonance. To check if this is the case, we computed the resonance angles defined as $\phi_i = (p + q)\lambda_2 - p\lambda_1 - q\omega_i$, where λ_i , $i = 1, 2$ is the mean longitude of each planet and ω_i , $i = 1, 2$ are their longitudes of perihelion, following [Millholland et al. \(2018\)](#). The behaviour of these angles can show whether a system is in resonance or not: if at least one of the angles oscillates then the system is inside the resonance. With this aim we conducted N-body integrations for 10^5 years, which is equivalent to ~ 4 million orbits of planet GJ 357 b. We used the nominal values given in Table 3 and 4, and a set of 10 initial inclinations for planet b ranging from 88.5° to 56.0° . For all of the scenarios tested, we found non-librating behaviour of the resonance angles, indicating that the system is not trapped in a 7:3 resonance.

5.3 Long-term stability

The set of results obtained so far allowed us to explore the long-term stability of the system in a smaller parameter space. Again we used the MEGNO criterion to find the most stable solutions, and we performed simulations up to 5×10^7 yr, storing the value of MEGNO every 1000 yr. We determined that any given system showed a trend towards chaotic behaviour when $|\Delta\langle Y(t) \rangle| > 0.5$, where $\Delta\langle Y(t) \rangle = 2.0 - \langle Y(t) \rangle$, i.e., when the integration started to diverge from values of 2.0, particularly beyond 0.5 units.

Next, we considered oscillations of $\langle Y(t) \rangle$ around 2.0 with amplitudes of < 0.5 as stable systems that need more integration time to clearly reveal their real trends. Two reasons prevented us from carrying out longer simulations of hundreds or thousands of Myr; first, the high computational cost, and second, the large number of errors propagated along the integrations will eventually imply that all the simulated scenarios show some degree of instability. Indeed, for very long-term integrations, a given chaotic behaviour might be caused by a lack of energy conservation accumulated at each time-step ([Rein & Tamayo 2015](#)).

We integrated the system considering co-planar orbits, where the two inner planets had circular orbits. We found that the system was stable for the total integration time, with a $|\Delta\langle Y \rangle| \sim 0.2$. Moreover, previously we found that planet GJ 357 b should have a low eccentricity in the 1σ uncertainty region to ensure the short-term stability of the system. Therefore, we explored different eccentricities: 0.072, 0.06, 0.05, 0.04, 0.02, 0.01, 0.005, and 0.001. We found that only very low eccentricities < 0.01 keeps our criteria of stable solutions. As such, we find that only near-circular configurations for planet GJ 357 b ensure long-term stability.

We moved on to examine the minimum inclination of GJ 357 b. Previous results regarding its short-term stability showed a minimum value of $i_b \sim 53^\circ$ when circular orbits were assumed for the two innermost planets b and c. However, during long-term integrations we found that the system became unstable when approaching 10^6 yr. As such, we explored the minimum values of i_b starting from 53° and increasing in increments of 2° until we found a stable solution. We find that for $i_b \sim 60^\circ$, the system is stable with $|\Delta\langle Y \rangle| \sim 0.3$. This means we can place strong constraints on the maximum mutual inclination of the two inner planets GJ 357 b and GJ 357 c of 28.5° , that yield a maximum mass for the planet GJ 357 b of $4.25 M_\oplus$.

We next explored the non-coplanarity of the outermost planet GJ 357 d. We considered the two inner planets as being coplanar, and residing in circular orbits. During the short-term stability analysis we found the minimum inclination of this planet as $i_d \sim 26^\circ$ for circular orbits, and $i_d \sim 32^\circ$ when $e_d = 0.033$. During these long-term integrations we found that for a circular configuration, the system becomes unstable in the range of $\sim 10^6$ yr. Following the same strategy described before, we progressively increased the inclination in increments of 2° to investigate its long-term stability. We find that for $i_b \sim 40^\circ$ or more, the system is stable with $|\Delta\langle Y \rangle| \sim 0.1$, i.e., the maximum mutual inclination between the two innermost planets and GJ 357 d is 48.5° , which implies a mass equivalent to $11.2 M_\oplus$ for this planet. On the other hand, in the case of a non-eccentric orbit for GJ 357 d when $i_d = 40^\circ$, we find the system becomes unstable in the range of $2\text{--}3 \times 10^7$ yr for eccentricities ranging from 0.01 to 0.033. When we tried with higher inclinations up to $i_d = 50^\circ$, we find that the system remains stable up to $4\text{--}5 \times 10^7$ yr, but its rapidly changing behaviour indicates instability at the limit of our integration. Therefore, at this moment, we can not unambiguously determine the maximum inclination in the case of eccentric orbits for GJ 357 d.

The set of results obtained in this section seems to favour a system of two super-Earths of $M_c = 2.087 M_\oplus$, $3.69 < M_b < 4.25 M_\oplus$ and a likely third mini-Neptune

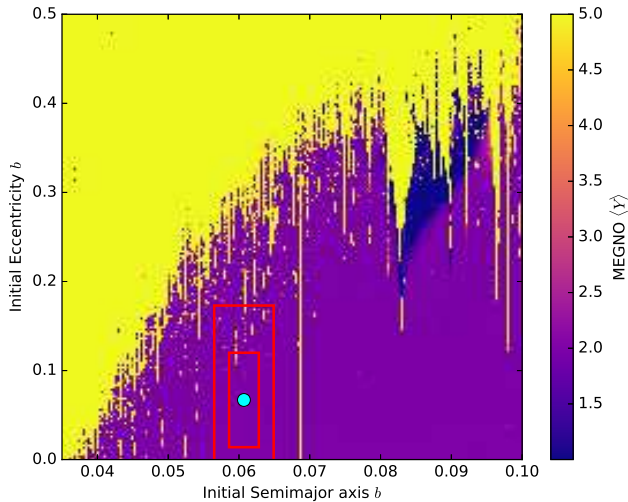


Figure 9. Dynamical analysis of planet GJ 357 b based on a MEGNO-map for a coplanar configuration. The size of the map is 200×200 pixels, which explores the $e_b - a_b$ parameter space. When $\langle Y(t) \rangle \rightarrow 2$ (purple shaded regions) quasi-periodic orbits are found, and chaotic systems are found when $\langle Y(t) \rangle \rightarrow 5$ (yellow shaded regions). The nominal value for GJ 357 b is shown by the blue marker, while the 1σ and 2σ uncertainties from the radial-velocity orbital solution are shown by the red boxes.

planet of $7.20 < M_d < 11.20 M_\oplus$, where the innermost planets GJ 357 c and GJ 357 b reside in near-circular orbits. The analysis of the b -parameter, and the normal trend for planetary systems to be nearly-coplanar, encouraged us to favour the hypothesis of near-coplanar orbits, which correspond to the minimum values in our mass ranges. However, we also found that the system might remain stable for non-coplanar configurations if the mutual inclinations do not exceed 28.5° for planets GJ 357 c and b, and 48.5° for planets GJ 357 c and d, which gives rise to the maximum values of the planetary masses.

With these strong upper mass constraints provided by the dynamic analysis, the GJ 357 planetary system becomes the only such multi-planet system that contains at least three planets that has been detected by RVs at this level of precision, that we are currently aware of (see Fig. 10). Transit photometry and transit timing variations have discovered the remaining systems. It can be seen in this figure that GJ 357 provides one of the most well constrained systems of planets in mass and period parameter space. This is largely due to the brightness of the target that has allowed a vast quantity of precision RVs to be observed, along with the detailed modelling effort that we provide.

When we compare the GJ 357 system to the other multi-planet systems shown in Fig. 10, we can see that the configuration is generally not typical of the population. Each of the planets gets more massive as a function of their orbital period. This likely reflects the bias inherent in the RV method, since most other systems show fairly vertical relationships, meaning the planet masses in these other systems are broadly similar, regardless of orbital period; there is no trend. In fact, Kepler-445 is the only system here where the outer planet is the least massive one, statistically. We can also see that there exists only one multi-planet system with

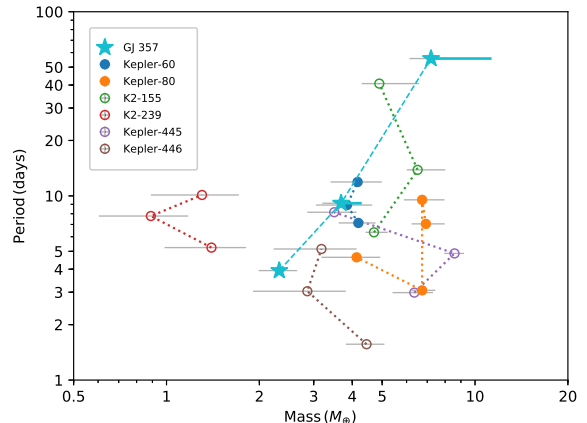


Figure 10. Mass versus orbital period for planetary systems hosting three or more low-mass planets with absolute masses measured to better than 43.5% (the uncertainty for GJ 357 d). Dashed lines connect each of the systems, uncertainties are shown as light grey error bars, and the thick and coloured lines mark the mass upper limits for GJ 357 b and d. Only GJ 357 has planets with absolute masses detected by radial-velocities (star symbols), the others have either been detected by transit photometry or transit timing variations (circular symbols). Open symbols mark those systems where the mass estimates were drawn from mass–radius relationships. The key in the plots highlights each of the planetary systems (K2-155–Díez Alonso et al. 2018a; K2-239–Díez Alonso et al. 2018b; Kepler-60–Steffen et al. 2013; Jontof-Hutter et al. 2016; Kepler-80–MacDonald et al. 2016; Kepler-445 & Kepler-446–Muirhead et al. 2015; Mann et al. 2017).

these constraints with masses below $2 M_\oplus$, K2-239. Actually, GJ 357c is the lowest mass planet discovered in such multi-planet systems, outside of K2-239. The plot also highlights that GJ 357 is only the third star to host such a rich and well constrained planetary system, (after Kepler-60 and Kepler-80), where masses were not drawn from mass–radius relationships.

6 CONCLUSIONS

The bright and nearby M dwarf star GJ 357 has recently been shown to host a low-mass transiting planetary system using precision photometry from the TESS mission and radial-velocity data. Our analysis of new precision radial-velocities from three different instruments, the HARPS, the HiRES, and the UVES results in evidence for a system of three small planets orbiting the star with periods of approximately 9, 4, and 56 days. Therefore, we confirm the detection of the planetary system in radial-velocity data independently of the TESS photometry. The detected planets have minimum masses of 3.68 ± 0.48 , 2.32 ± 0.33 , and $7.20 \pm 1.07 M_\oplus$ for the planets GJ 357b,c, and d, respectively. When we simultaneously fit the TESS lightcurve with the radial-velocities, we find tight constraints on the mass, radius, and density of $2.248^{+0.117}_{-0.120} M_\oplus$, $1.167^{+0.037}_{-0.036} R_\oplus$, and $7.757^{+0.889}_{-0.789} \text{gcm}^{-3}$ respectively, for planet GJ 357c. Com-

parison to structure models indicates the planet is a predominantly iron-rich world.

In order to better understanding the real nature of this system and unveil its most likely dynamical configuration, we combined both short- and long-term simulations to constrain the planetary masses, eccentricities, and inclinations in terms of their stability based on the MEGNO criterion. The simulations revealed the following:

(i) The system is likely coplanar, or near-coplanar, since the analysis of the impact parameter revealed that closely coplanar orbits would render the two outer planets such that they would not be expected to transit the star.

(ii) The two innermost planets should be in near-circular orbits. Indeed, we found that to ensure the long-term stability of the system the eccentricity of planet GJ 357b should be $\lesssim 0.01$.

(iii) The two non-transiting planets, GJ 357b and d, can not have inclinations exceeding 60° and 40° , respectively. This allows upper limits to be placed on the masses of these planets of $4.25 M_\oplus$ and $11.2 M_\oplus$, respectively.

The GJ 357 planetary system adds to the growing number of systems orbiting some of the smallest and nearest stars. The system we have uncovered appears to be composed of a mix of rocky planets and a mini-Neptune. This is the only such multi-planet system with well constrained masses detected by RVs, and only the second system that does not apply empirical or theoretical mass–radius relationships to calculate the planetary masses. Furthermore, GJ 357 is significantly brighter than the host stars of these other well constrained planetary systems, which offers significant advantages for future understanding of planetary dynamics and atmospheric characterisation. Detailed analyses of the planetary properties with additional observations, whilst searching for more companions on longer period orbits, or hidden worlds in the stable dynamical cavity between GJ 357b and d, can be made without large investments of telescope time. This system provides us with a benchmark laboratory to understand the formation and evolutionary processes of small planets orbiting small stars.

ACKNOWLEDGMENTS

We thank the referee Stephen Kane for his detailed review of the manuscript that helped tighten-up various sections of our work. JSJ and MT acknowledges funding by Fondecyt through grant 1161218 and partial support from CATA-Basal (PB06, Conicyt). ZMB acknowledges CONICYT-FONDECYT/Chile Postdoctorado 3180405. JIV acknowledges support of CONICYT-PFCHA/Doctorado Nacional-21191829, Chile. MRD acknowledges support of CONICYT-PFCHA/Doctorado Nacional-21140646, Chile and Proyecto Basal AFB-170002. FJP and JCS acknowledges funding support from Spanish public funds for research under projects ESP2017-87676-C5-2-R.

REFERENCES

- Adibekyan V. Z., Sousa S. G., Santos N. C., Delgado Mena E., González Hernández J. I., Israelian G., Mayor M., Khachaturyan G., 2012, *A&A*, **545**, A32
- Alberti T., Carbone V., Lepreti F., Vecchio A., 2017, *ApJ*, **844**, 19
- Anglada-Escudé G., Butler R. P., 2012, *ApJS*, **200**, 15
- Anglada-Escudé G., et al., 2013, *A&A*, **556**, A126
- Anglada-Escudé G., et al., 2016, *Nature*, **536**, 437
- Astudillo-Defru N., Delfosse X., Bonfils X., Forveille T., Lovis C., Rameau J., 2017, *A&A*, **600**, A13
- Ballard S., 2019, *AJ*, **157**, 113
- Berdiñas Z. M., Rodríguez-López C., Amado P. J., Anglada-Escudé G., Barnes J. R., MacDonald J., Zechmeister M., Sarmiento L. F., 2017, *MNRAS*, **469**, 4268
- Bonfils X., et al., 2005, *A&A*, **443**, L15
- Bonfils X., et al., 2013, *A&A*, **549**, A109
- Borucki W. J., et al., 2010, *Science*, **327**, 977
- Buchner J., et al., 2014, *A&A*, **564**, A125
- Burdanov A. Y., et al., 2019, arXiv e-prints,
- Butler R. P., et al., 2017, *AJ*, **153**, 208
- Cincotta P., Simó C., 1999, *Celestial Mechanics and Dynamical Astronomy*, **73**, 195
- Cincotta P. M., Simó C., 2000, *Astronomy and Astrophysics Supplement Series*, **147**, 205
- Cincotta P. M., Giordano C. M., Simó C., 2003, *Physica D Nonlinear Phenomena*, **182**, 151
- Contro B., Horner J., Wittenmyer R. A., Marshall J. P., Hinse T. C., 2016, *MNRAS*, **463**, 191
- Díaz M. R., et al., 2018, *AJ*, **155**, 126
- Díez Alonso E., et al., 2018a, *MNRAS*, **476**, L50
- Díez Alonso E., et al., 2018b, *MNRAS*, **480**, L1
- Dressing C. D., Charbonneau D., 2015, *ApJ*, **807**, 45
- Ducrot E., et al., 2018, *AJ*, **156**, 218
- Espinoza N., Kossakowski D., Brahm R., 2018, arXiv e-prints, p. arXiv:1812.08549
- Fabrycky D. C., et al., 2014, *ApJ*, **790**, 146
- Feng F., Tuomi M., Jones H. R. A., Butler R. P., Vogt S., 2016, *MNRAS*, **461**, 2440
- Feng F., Tuomi M., Jones H. R. A., Barnes J., Anglada-Escudé G., Vogt S. S., Butler R. P., 2017, *AJ*, **154**, 135
- Feroz F., Hobson M. P., Bridges M., 2009, *MNRAS*, **398**, 1601
- Figueira P., et al., 2012, *A&A*, **541**, A139
- Fischer D. A., Valenti J., 2005, *ApJ*, **622**, 1102
- Foreman-Mackey D., Hogg D. W., Lang D., Goodman J., 2013, *PASP*, **125**, 306
- Foreman-Mackey D., Agol E., Angus R., Ambikasaran S., 2017, *AJ*, **154**, 220
- Forveille T., et al., 2009, *A&A*, **493**, 645
- Fulton B. J., Petigura E. A., Blunt S., Sinukoff E., 2018, *PASP*, **130**, 044504
- Gaia Collaboration et al., 2016, *A&A*, **595**, A1
- Gaia Collaboration et al., 2018, doi:10.1051/0004-6361/201833051, **616**, A1
- Gillon M., et al., 2017, *Nature*, **542**, 456
- Günther M. N., et al., 2019, arXiv e-prints, p. arXiv:1903.06107
- Haario H., Saksman E., Tamminen J., 2001, *Bernoulli*, **7**, 223
- Haario H., Laine M., Mira A., Saksman E., 2006, *Statistics and Computing*, **16**, 339
- Hastings W. K., 1970, *Biometrika*, **57**, 97
- Hinse T. C., Christou A. A., Alvarellos J. L. A., Goździewski K., 2010, *MNRAS*, **404**, 837
- Hinse T. C., Haghighipour N., Kostov V. B., Goździewski K., 2015, *ApJ*, **799**, 88
- Houdebine E. R., Mullan D. J., Bercu B., Paletou F., Gebran M., 2017, *ApJ*, **837**, 96
- Jenkins J. S., Jones H. R. A., Pavlenko Y., Pinfield D. J., Barnes J. R., Lyubchik Y., 2008, *A&A*, **485**, 571

- Jenkins J. S., et al., 2009, *MNRAS*, **398**, 911
- Jenkins J. S., et al., 2011, *A&A*, **531**, A8
- Jenkins J. M., et al., 2016, in *Software and Cyberinfrastructure for Astronomy IV*. p. 99133E, doi:10.1117/12.2233418
- Jenkins J. S., et al., 2017, *MNRAS*, **466**, 443
- Johnson J. A., Aller K. M., Howard A. W., Crepp J. R., 2010, *PASP*, **122**, 905
- Jontof-Hutter D., et al., 2016, *ApJ*, **820**, 39
- Kass R. E., Raftery A. E., 1995, *J. Am. Stat. Ass.*, **430**, 773
- Kopparapu R. K., 2013, *ApJL*, **767**, L8
- Kreidberg L., 2015, *Publications of the Astronomical Society of the Pacific*, **127**, 1161
- Laughlin G., Bodenheimer P., Adams F. C., 2004, *ApJL*, **612**, L73
- Lee M. H., Peale S. J., Pfahl E., Ward W. R., 2007, *Icarus*, **190**, 103
- Libert A. S., Tsiganis K., 2009a, *MNRAS*, **400**, 1373
- Libert A. S., Tsiganis K., 2009b, *A&A*, **493**, 677
- Liddle A. R., 2007, *MNRAS*, **377**, L74
- Luque R., et al., 2019, arXiv e-prints,
- MacDonald M. G., et al., 2016, *AJ*, **152**, 105
- Mann A. W., et al., 2017, *AJ*, **153**, 267
- Mayor M., et al., 2009, *A&A*, **507**, 487
- Metropolis N., Rosenbluth A. W., Rosenbluth M. N., Teller A. H., Teller E., 1953, *J. Chem. Phys.*, **21**, 1087
- Miles-Pérez P. A., Zapatero Osorio M. R., Pallé E., Metchev S. A., 2019, *MNRAS*, **484**, L38
- Millholland S., et al., 2018, *AJ*, **155**, 106
- Montes D., et al., 2018, *MNRAS*, **479**, 1332
- Moran S. E., Hörst S. M., Batalha N. E., Lewis N. K., Wakeford H. R., 2018, *AJ*, **156**, 252
- Muirhead P. S., et al., 2015, *ApJ*, **801**, 18
- Muirhead P. S., Dressing C. D., Mann A. W., Rojas-Ayala B., Lépine S., Paegert M., De Lee N., Oelkers R., 2018, *AJ*, **155**, 180
- Neves V., Bonfils X., Santos N. C., Delfosse X., Forveille T., Allard F., Udry S., 2014, *A&A*, **568**, A121
- Peña Rojas P. A., Jenkins J. S., 2019, *A&A*, p. in prep
- Perryman M. A. C., Lindegren L., Kovalevsky J., et al. 1997, *A&A*, **323**, L49
- Pojmanski G., 1997, *Acta Astronomica*, **47**, 467
- Rein H., Liu S.-F., 2012, *A&A*, **537**, A128
- Rein H., Tamayo D., 2015, *MNRAS*, **452**, 376
- Ribas I., et al., 2018, *Nature*, **563**, 365
- Ricker G. R., et al., 2015, *Journal of Astronomical Telescopes, Instruments, and Systems*, **1**, 014003
- Rojas-Ayala B., Covey K. R., Muirhead P. S., Lloyd J. P., 2010, *ApJL*, **720**, L113
- Savitzky A., Golay M. J. E., 1964, *Analytical Chemistry*, **36**, 1627
- Schlaufman K. C., Laughlin G., 2010, *A&A*, **519**, A105
- Schöfer P., et al., 2019, *A&A*, **623**, A44
- Sousa S. G., Santos N. C., Israelian G., Mayor M., Udry S., 2011, *A&A*, **533**, A141
- Stassun K. G., et al., 2018, *AJ*, **156**, 102
- Steffen J. H., et al., 2013, *MNRAS*, **428**, 1077
- Tremaine S., Dong S., 2012, *AJ*, **143**, 94
- Tuomi M., 2011, *A&A*, **528**, L5
- Tuomi M., Jones H. R. A., Barnes J. R., Anglada-Escudé G., Jenkins J. S., 2014, *MNRAS*, **441**, 1545
- Tuomi M., Jones H. R. A., Barnes J. R., Anglada-Escudé G., Butler R. P., Kiraga M., Vogt S. S., 2018, *AJ*, **155**, 192
- Tuomi M., Jones H. R. A., Anglada-Escudé G. e. a., 2019, *ApJ*
- Winn J. N., 2010, *Exoplanet Transits and Occultations*. pp 55–77
- Zechmeister M., Kürster M., 2009, *A&A*, **496**, 577
- Zechmeister M., Kürster M., Endl M., 2009, *A&A*, **505**, 859